Self-Organized Anodic TiO_2 Nanotube Arrays Functionalized by Iron Oxide Nanoparticles

Athanassios I. Kontos, Vlassis Likodimos, Thomas Stergiopoulos, Dimitrios S. Tsoukleris, and Polycarpos Falaras*

Institute of Physical Chemistry, NCSR Demokritos, 153 10, Aghia Paraskevi Attikis, Athens, Greece

Ioannis Rabias and George Papavassiliou

Institute of Materials Science, NCSR Demokritos, 153 10, Aghia Paraskevi Attikis, Athens, Greece

Doohun Kim, Julia Kunze, and Patrik Schmuki

Department of Materials Science, WW4-LKO, University of Erlangen-Nuremberg, Martensstrasse 7 D-91058 Erlangen, Germany

Received September 16, 2008. Revised Manuscript Received December 16, 2008

Surface functionalization of self-organized TiO_2 nanotube (NT) arrays produced by electrochemical anodization is implemented by dextrin-coated iron-oxide nanoparticles leading to a composite semiconductor nanostructure. The morphological and structural properties are studied by electron and atomic force microscopy, X-ray diffraction, X-ray photoelectron, and resonance micro-Raman spectroscopies revealing successful deposition of maghemite (γ-Fe_2O_3) nanoparticles on the nanotube walls. The nanocomposite surface simultaneously exhibits high photocatalytic activity for the degradation of model pollutants under UV irradiation at relatively low loading levels of the γ-Fe_2O_3 nanoparticles and light-independent wetting properties, as the initially superhydrophilic surface is converted to a moderately hydrophilic substrate, while obtaining an additional functionality through the magnetic field response of the iron-oxide component that shows appreciable magnetization anisotropy. Electrochemical impedance investigation including Mott−Schottky analysis attests to a significant improvement of the interfacial electron-transfer kinetics together with a modification of the surface chemistry for the functionalized TiO_2 nanotubes, promoting electron−hole separation through the polyhydroxyl dextrin shell that mediates charge transfer between the constituent semiconductor oxides and validating their improved photocatalytic performance. These composite nanotubular materials offer the opportunity of advanced applications, where the unique photoinduced reactivity, the controlled wetting behavior, and the magnetic field response can be effectively combined.

1. Introduction

Titanium dioxide (TiO_2) has attracted a lot of interest because of its unique photoinduced reactivity amply explored for applications in environmental photocatalysis,[1,2] solar energy conversion,[3] and the more recently discovered effect of light-induced amphiphilicity, involving the control of its surface wettability by UV radiation that markedly expanded its application potential.[4] Current research efforts focus on tailoring the morphology and surface complexity of TiO_2 nanomaterials, tuning their electronic properties via transition metal ion and anionic doping, and improving their photoinduced performance through surface modification/sensitization by metal nanoparticles, organic dyes, as well as narrow band gap semiconductors.[5,6]

Iron oxide nanoparticles represent another important class of nanostructured materials, whose unique size-dependent magnetic properties,[7] along with their nontoxicity, low cost, and versatile synthesis, hold promise for a broad range of technological applications, a prominent one being their utilization in biomedicine and biotechnology, including drug delivery, sensing and separation of biological targets, contrast enhancement in magnetic resonance imaging and hyperthermia agents.[8,9] Intensive research is accordingly carried out in tailoring the morphology and surface functionalization of iron nanoparticles, which are crucial factors in attaining the

* Corresponding author. E-mail: papi@chem.demokritos.gr. Tel: 30-210-6503644. Fax: 30-210-6511766.

(1) Hashimoto, K.; Irie, H.; Fujishima, A. *Jpn. J. Appl. Phys* **2005**, *44*, 8269.
(2) Choi, H.; Sofranko, A. C.; Dionysiou, D. D. *Adv. Funct. Mater.* **2006**, *16*, 1067.
(3) Grätzel, M. *Nature* **2001**, *414*, 338.
(4) Wang, R.; Hashimoto, K.; Fujishima, A.; Chikuni, M.; Kojima, E.; Kitamura, A.; Shimohigoshi, M.; Watanabe, T. *Nature* **1997**, *388*, 431.
(5) Carp, O.; Huisman, C. L.; Reller, A. *Prog. Solid State Chem.* **2004**, *32*, 33.
(6) Chen, X.; Mao, S. S. *Chem. Rev.* **2007**, *107*, 2891.
(7) Batlle, X.; Labarta, A. *J. Phys. D: Appl. Phys.* **2002**, *35*, R15.
(8) (a) Alivisatos, A. P. *Nat. Biotechnol.* **2004**, *22*, 47. (b) Rosi, N. L.; Mirkin, C. A. *Chem. Rev.* **2005**, *105*, 1547. (c) Jun, Y.-W.; Seo, J.-W.; Cheon, J. *Acc. Chem. Res.* **2008**, *41*, 179.
(9) Pankhurst, Q. A.; Connolly, J.; Jones, S. K.; Dobson, J. *J. Phys. D: Appl. Phys.* **2003**, *36*, R167.

10.1021/cm802495p CCC: $40.75
Published on Web 01/22/2009

specific targeting ability and functionality required for biomedical applications.[10]

Successful synthesis of highly ordered TiO_2 nanotube (NT) arrays by electrochemical anodization of titanium has recently provided a straightforward fabrication route to a vertically oriented architecture offering a large internal surface area and more efficient light harvesting that may potentially outweigh the performance of nanoparticulate TiO_2.[11] Soon after the first reports of self-organized TiO_2 NT layers with tube lengths of ~500 nm,[11] thorough studies on the optimization of the electrochemical growth conditions have yielded high-aspect-ratio NT arrays reaching the millimeter scale.[12−16] From the applied perspective, TiO_2 NTs have been found to promote water photocleavage with high photoconversion efficiency under UV radiation,[17] and exhibit excellent photocatalytic properties, exceeding that of TiO_2 nanoparticle films, utilized in most practical applications.[18−20] TiO_2 NT layers have shown superhydrophilic behavior, which can be controllably switched to superhydrophobic by attaching self-assembled organic monolayers and by varying the tube diameter.[21] Incorporation of TiO_2 NTs arrays in dye-sensitized solar cells has also shown considerably high charge collection efficiencies, where significant improvement is anticipated by modifying the morphological characteristics of the NT architecture.[22−25] Moreover, doping of TiO_2 NTs with nitrogen,[26] carbon,[27] and boron[28] heteroatoms has been recently reported to produce enhanced photocurrents in both the UV and visible ranges, whereas loading of NT layers with transition metals has been found to raise their photocatalytic activity.[29]

A further step toward improving the functionality of TiO_2 nanomaterials has been recently devised through the growth of binary nanocrystals comprising spherical γ-Fe_2O_3 magnetic nanoparticles attached on anatase TiO_2 nanorods.[30] Such a hybrid nanostructure offers the prospect of reinforced applications through the combined action of the two oxide nanomaterials, where the biomedical functionality of the magnetic nanoparticles can be fruitfully exploited with the high oxidizing potential of TiO_2. Very recently, loading of sulfur-doped titanate nanotubes with iron oxide nanoparticles has been reported to improve significantly the photocatalytic activity for the oxidation of acetaldehyde through efficient charge separation of the photoexcited electrons and holes.[31] Moreover, the self-organized, highly ordered tubular architecture of anodic TiO_2 NTs has been shown to be an excellent substrate for the adherence, spreading and growth of living cells that promotes cellular activity, when the tube morphological characteristics are appropriately tuned,[32] and most importantly that anodic TiO_2 NTs can act as efficient photocatalysts for the photoinduced killing of cancer cells.[33]

An important aspect in the photocatalytic applications of titanium dioxide is that the self-cleaning action, which involves photodegradation, is always accompanied by enhanced surface photoinduced superhydrophilicity.[1] These functionalities (photocatalytic activity and wetting behavior) are interrelated and their separation, usually necessary for process optimization, remains a challenging task.[34] To explore the advantageous characteristics of both self-organized TiO_2 NT arrays and iron oxide nanoparticles we report, in the present paper, on the surface functionalization of anodized TiO_2 NTs arrays by dextrin-coated iron oxide nanoparticles. Such a modification provides additional functionalities in the oriented TiO_2 NT layers through the inorgano-polymeric surface additives leading to a hybrid semiconductor oxide nanocomposite. The morphology, phase composition, and electrochemical properties of the composite nanomaterials are systematically investigated by scanning electron and atomic force microscopy, X-ray diffraction, X-ray photoelectron spectroscopy, resonance micro-Raman and diffuse reflectance UV−vis spectroscopy together with electrochemical impedance spectroscopy and Mott−Schottky analysis. Successful deposition of maghemite (γ-Fe_2O_3) nanoparticles on the NT walls is confirmed, whereas the photochemical properties of the nanocomposite are systematically explored in terms of the iron-oxide concentration in order to assess its application potential. High photocatalytic activity is thus obtained under appropriate loading of γ-Fe_2O_3

(10) (a) Yi, D. K.; Selvan, S. T.; Lee, S. S.; Papaefthymiou, G. C.; Kundaliya, D.; Ying, J. Y. *J. Am. Chem. Soc.* **2005**, *127*, 4991. (b) Huh, Y.-M.; Jun, Y.; Song, H.-T.; Kim, S.; Choi, J.; Lee, J.-H.; Yoon, S.; Kim, K.-S.; Shin, J.-S.; Suh, J.-S.; Cheon, J. *J. Am. Chem. Soc.* **2005**, *127*, 12387. (c) Yi, D. K.; Lee, S. S.; Papaefthymiou, G. C.; Ying, J. Y. *Chem. Mater.* **2006**, *18*, 614.
(11) Macak, J. M.; Tsuchiya, H.; Ghicov, A.; Yasuda, K.; Hahn, R.; Bauer, S.; Schmuki, P. *Curr. Opin. Solid State Mater. Sci.* **2007**, *11*, 3.
(12) Macak, J. M.; Tsuchiya, H.; Taveira, L.; Aldabergerova, S.; Schmuki, P. *Angew. Chem., Int. Ed.* **2005**, *44*, 7463.
(13) Albu, P. S.; Ghicov, A.; Macak, J. M.; Schmuki, P. *Phys. Stat. Sol. (RRL)* **2007**, *1*, R65.
(14) Paulose, M.; Prakasam, H. E.; Varghese, O. K.; Peng, L.; Popat, K. D.; Mor, G. K.; Desai, T. A.; Grimes, C. A. *J. Phys. Chem. C* **2007**, *111*, 14992.
(15) Feng, X.; Macak, J. M.; Schmuki, P. *Chem. Mater.* **2007**, *19*, 1534.
(16) Wang, J.; Lin, Z. *Chem. Mater.* **2008**, *20*, 1257.
(17) Mor, G. K.; Shankar, K.; Paulose, M.; Varghese, O. K.; Grimes, C. A. *Nano Lett.* **2005**, *5*, 191.
(18) Macak, J. M.; Zlamal, M.; Krysa, J.; Schmuki, P. *Small* **2007**, *3*, 300.
(19) Zhuang, H.-F.; Lin, C.-J.; Lai, Y.-K.; Sun, L.; Li, J. *Environ. Sci. Technol.* **2007**, *41*, 4735.
(20) Liu, Z.; Zhang, X.; Nishimoto, S.; Jin, M.; Tryk, D. A.; Murakami, T.; Fujishima, A. *J. Phys. Chem. C* **2008**, *112*, 253.
(21) Balaur, E.; Macak, J. M.; Tsuchiya, H.; Schmuki, P. *J. Mater. Chem.* **2005**, *15*, 4488.
(22) Zhu, K.; Neale, N. R.; Miedaner, A.; Frank, A. J. *Nano Lett.* **2007**, *7*, 69.
(23) Mor, G. K.; Shankar, K.; Paulose, M.; Varghese, O. K.; Grimes, C. A. *Nano Lett.* **2006**, *6*, 215.
(24) Stergiopoulos, T.; Ghicov, A.; Likodimos, V.; Tsoukleris, D. S.; Kunze, J.; Schmuki, P.; Falaras, P. *Nanotechnology* **2008**, *19*, 235602.
(25) Kuang, D.; Brillet, J.; Chen, P.; Takata, M.; Uchida, S.; Miura, H.; Sumioka, K.; Zakeeruddin, S. M.; Grätzel, M. *ACS Nano* **2008**, *2*, 1113.
(26) Ghicov, A.; Macak, J. M.; Tsuchiya, H.; Kunze, J.; Haeublein, V.; Frey, L.; Schmuki, P. *Nano Lett.* **2006**, *6*, 1080.
(27) Park, J. H.; Kim, S.; Bard, A. J. *Nano Lett.* **2006**, *6*, 24.
(28) Lu, N.; Quan, X.; Li, J. Y.; Chen, S.; Yu, H. T.; Chen, G. H. *J. Phys. Chem. C* **2007**, *111*, 11836.
(29) Paramasivam, I.; Macak, J. M.; Schmuki, P. *Electrochem. Commun.* **2008**, *10*, 71.
(30) Buonsanti, R.; Grillo, V.; Carlino, E.; Giannini, C.; Curri, M. L.; Innocenti, C.; Sangregorio, C.; Achterhold, K.; Parak, F. G.; Agostiano, A.; Cozzoli, P. D. *J. Am. Chem. Soc.* **2006**, *128*, 16953.
(31) Nishijima, K.; Fujisawa, Y.; Murakami, N.; Tsubota, T.; Ohno, T. *Appl. Catal. B* **2008**, *84*, 584.
(32) Park, J.; Bauer, S.; Von der Mark, K.; Schmuki, P. *Nano Lett.* **2007**, *7*, 1686.
(33) Kalbacova, M.; Macak, J. M.; Schmidt-Stein, F.; Mierke, C. T.; Schmuki, P. *Phys. Status Solidi* **2008**, *2*, 194.
(34) Kontos, A. I.; Kontos, A. G.; Tsoukleris, D. S.; Vlachos, G. D.; Falaras, P. *Thin Solid Films* **2007**, *515*, 7370.

nanoparticles together with the modification of the initially superhydrophilic surface of the TiO_2 NT arrays to a moderately hydrophilic substrate, while adding the magnetic component. Such an advantageous combination of the two constituent oxide nanostructures leads to effective separation of photocatalytic and wetting properties that renders these nanocomposite materials very attractive for self-cleaning and biomedical applications.

2. Experimental Section

2.1. Synthesis of TiO_2 Nanotube Arrays. Self-organized porous TiO_2 NT layers were prepared by electrochemical anodization of titanium foils (0.1 mm thickness, 99.6% purity, Goodfellow, England) polished and chemically cleaned following sonication in acetone, isopropanol and methanol, in 1 M (NaH_2PO_4 and H_3PO_4) + 0.3 wt % HF using a high-voltage potentiostat (Jaissle IMP 88). The potential was initially ramped with a sweep rate of 0.5 V/s from 0 to 20 V and then kept constant for 2 h. After the electrochemical treatment the samples were rinsed with deionized water and dried in a nitrogen stream. Thermal annealing was performed in ambient air at 450 °C for 1 h with heating and cooling rates of 30 °C/min (JetFirst, Jiplec).

2.2. Synthesis and Deposition of Iron Oxide Nanoparticles. A dispersion of fine iron oxide nanoparticles (Fe_xO_y) coated with dextrin was synthesized by the reaction of ferric chloride and ferrous chloride in the presence of ammonia, using the coprecipitation method.[35] The nominal molecular weight of the dextrin ($C_{18}H_{32}O_{16}$) used was 504.44 (g/mol). Aqueous solutions of 0.1 M Fe(III) (30 mL) and 0.1 M Fe(II) (15 mL) were mixed, and 3 mL of 5 M ammonia solution was added dropwise over 1 min while the solution was stirred. The stirring was continued for 20 min under a nitrogen-gas atmosphere. The particles obtained were washed 3 times using ultracentrifugation with nitrogen purged water. The iron oxide nanoparticle yield, determined by weighing the lyophilized sample, was 400 mg. Formulations of iron oxide nanoparticles were developed, first by optimizing the amount of dextrin coating required to coat the iron oxide nanoparticles completely, and then by optimizing the amount of coating required to form an aqueous dispersion of dextrin coated nanoparticles. The formulations were heated to 60 °C while being stirred for 30 min and then cooled to room temperature. The black precipitate thus obtained was washed twice with 15 mL of water. The precipitate was lyophilized for 2 days at −60 °C. Finally, the colloidal suspension was filtered through a 0.22 μm pore size filter. To perform the surface modification, we dipped the TiO_2 NTs in iron oxide aqueous suspensions of variable concentrations in the range of 1−10 mg/mL, always subjecting them to ultrasound sonication before the dip coating process. After being dipped, the samples were thoroughly washed with ultrapure water and dried under a N_2 stream.

2.3. Characterization Techniques. The size and shape of the iron oxide particles were determined by high-resolution transmission electron microscopy (HRTEM) using a JEOL 2011 electron microscope, operated at 200 kV. HRTEM measurements were performed on carbon-coated copper grids, where a drop of an iron-oxide solution in ethanol was deposited, following treatment in an ultrasonic bath in order to separate aggregated particles. The morphology and chemical composition of the nanocomposite materials were studied by field-emission scanning electron microscopy (FE-SEM) (Hitachi SEM FE 4800), atomic force microscopy (DI Nanoscope III) operating in tapping mode, X-ray powder diffraction (XRD) (Phillips X'pert-MPD PW 3040) using Cu Kα radiation, X-ray photoelectron spectroscopy (XPS) (PHI 5600, Perkin-Elmer, Al Kα) and micro-Raman spectroscopy (Renishaw inVia Reflex). Raman spectra were collected in backscattering configuration, using the excitation lines of an Ar^+ ion laser (λ=514 nm) and a high power near-infrared (NIR) diode laser (λ = 785 nm). The laser beam was focused on the sample using a 50× objective producing a spot of ~1.5 μm size.

Diffuse reflectance UV−vis measurements were performed on a Hitachi U-4001 spectrometer equipped with an integrating sphere. The diffuse reflectance spectra were measured on samples cut in the form of circular plates of 1 cm diameter fully covered with the TiO_2 NT arrays. The absorbance has been subsequently derived in Kubelka−Munk units after subtraction of the specular component. Electrochemical impedance spectroscopy and Mott−Schottky analysis have been carried out in a 0.1 M Na_2SO_4 solution. The impedance was measured at 0 V constant potential and ± 10 mV amplitude of the sinusoidal signal, with a universal electrochemical interface and an impedance spectrum analyzer Zahner IM6d. For Mott−Schottky measurements, the potential was scanned with 0.1 V per step (forward −0.4 to 1 V, backward 1 to −0.4 V) at 30 Hz. The potentials are given vs Ag/AgCl reference electrode. Magnetization measurements were carried out at room temperature with the magnetic field applied parallel and perpendicular to the nanotube axis using a vibrating sample magnetometer (DANFYSIK System 8000) at magnetic fields up to 20 kOe.

2.4. Photocatalytic and Wetting Experiments. The photocatalytic activity of the TiO_2 NT arrays was evaluated by the degradation of the methyl orange (4-[(4-dimethylamino)phenyl-azo]) (MO) azo-dye. Photocatalytic experiments were carried out in round-bottom quartz cells introduced in a homemade photoreactor and irradiated by four F15W/T8 light tubes (Sylvania GTE). This UVC source shows maximum irradiation at 254 nm, emitting 1.5 mW/cm^2 on the photocatalyst surface (0.3 × 0.7 cm^2). All experiments were performed under continuous stirring, using 4 mL of 2×10^{-5} M aqueous solution, which was previously saturated with oxygen by bubbling the solution with O_2 for 2 h. Analytical determination of the azo-dye was carried out spectrophotometrically at 466.5 nm with an extinction coefficient of 25100 M^{-1} cm^{-1}. The hydrophilic properties were evaluated by measuring the advancing contact angle between the NT layers and water droplets as a function of the UV (254 and 350 nm) illumination time. Advancing water contact angle measurements were performed at room temperature by the extension method using a horizontal microscope with a protractor eyepiece (Contact Angle Meter-CAM 100, KSV Instruments Ltd.).

3. Results and Discussion

3.1. Morphology and Structure. The surface characteristics depend strongly on the functionalization of the materials. Figure 1 shows a TEM image of the iron-oxide (Fe_xO_y) nanoparticle dispersion and representative SEM micrographs of the bare TiO_2 NT array and its morphological variation after dip coating in 5 and 10 mg/mL aqueous suspensions of Fe_xO_y nanoparticles. The iron oxide nanoparticles exhibit rounded corners with rectangular or roughly ellipsoid shapes having sizes in the range of 7 to 15 nm (Figure 1a), while the self-organized TiO_2 layer consists of a dense array of vertically aligned NTs with tube diameter of ~100 nm and length of approximately 1 μm (Figure 1b). After dip coating the NT samples in the Fe_xO_y nanoparticle suspensions, the tube walls become decorated with aggregates of fine nanoparticles that penetrate into the TiO_2 NT pores (Figure 1c). In some areas, clusters of iron oxide nanoparticles are formed in the interior of the tube openings (see Figure S1 in the

(35) Massart, R.; Cabuil, V. *J. Phys. Chem.* **1987**, *84*, 967.

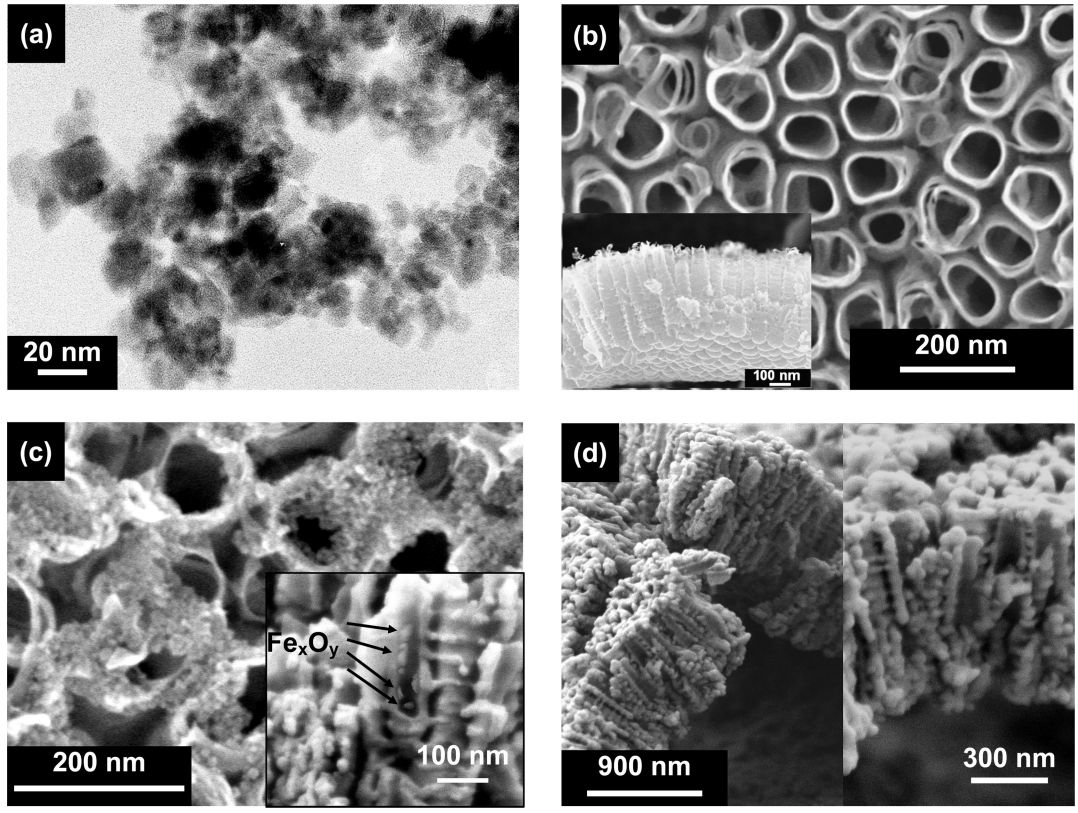

Figure 1. (a) Low-magnification HRTEM micrograph of the Fe_xO_y nanoparticles. (b) Top and side (inset) view SEM images of the unmodified TiO_2 NTs. (c) Top and side (inset) view SEM images of the TiO_2 NTs after deposition of the iron oxide nanoparticles (5 mg/mL). Arrows indicate iron oxide clusters. (d) SEM images of modified TiO_2 NTs after deposition of the iron oxide nanoparticles at high concentrations (10 mg/mL).

Supporting Information). Similar morphology of the composite nanostructure is observed after depositing Fe_xO_y nanoparticles from aqueous suspensions of higher concentrations (10 mg/mL), leading to a thicker layer of iron oxide aggregates on the TiO_2 NT walls as well as to a narrowing of the tube pores (Figure 1d).

The surface morphology, roughness, and complexity of the nanomaterials were further studied by atomic force microscopy (AFM). It is important to notice the extreme difficulty to perform such an examination, due to the nanotubular nature of the samples. Figure 2 shows the corresponding top-view AFM images of the bare TiO_2 NTs compared to the modified ones with the Fe_xO_y nanoparticles. Figure 2a reveals a highly textured (R_{ms} = 30.1 nm = the standard deviation of the Z values, Z being the total height range analyzed) and complex surface in the form of a network of oriented, well defined and interconnected titania tubes. Fractal analysis performed using theV423r3 algorithm confirms both high frequency and geometric complexity of surface features. The fractal dimension (D_f) of the surface is found to be as high as 2.35, proving its fractal behavior together with a self-affine and self-similar character as a consequence of the anodic oxidation process. Surface modification of the NT surface results in a highly different surface configuration, as shown in Figure 2b. Following a chaotic deposition, Fe_xO_y nanoparticles are present both inside and outside the titania tubes, thus decreasing roughness (R_{ms} = 19 nm) and transforming the material surface to a nonfractal one (D_f = 2.05).

Figure 3 compares the XRD patterns of the NT array before and after depositing the iron oxide nanoparticles (5 mg/ml solution). The bare substrate shows the presence of crystalline anatase TiO_2 ($I4_1/amd$) identified mainly by the (101) reflection, whereas additional diffraction peaks emerge after loading with the Fe_xO_y nanoparticles. Comparison with the standard XRD powder patterns of iron oxide and oxyhydroxide phases, allows the identification of a major cubic spinel phase. This indicates the presence of maghemite γ-Fe_2O_3 (space group $P4_132$) and/or magnetite Fe_3O_4 (space group $Fd3m$), exhibiting nearly identical XRD patterns, which cannot be discriminated because of the weak intensity and broadening of the diffraction peaks. Figure 4 shows the corresponding XPS spectra of the Fe_xO_y/TiO_2 NTs in the Fe 2p core-level region. The background has been calculated using the Shirley method and the electron takeoff angle has been adjusted to 45° with respect to the surface normal. Two weak but well-defined peaks at approximately 710.8 and 724.2 eV are observed, in agreement with the typical values of the Fe $2p_{3/2}$ and $2p_{1/2}$ core-level XPS peaks for ferric oxides.[36,37] In addition, the main Fe $2p_{3/2}$ and $2p_{1/2}$ peaks are accompanied by weak satellite structures on their high binding energy side, about 8 eV above the respective Fe 2p line. Such a spectrum is typical of Fe_2O_3 oxides (α- and γ-Fe_2O_3 polymorphs),[37] as well as iron oxyhydroxides,[36] whose differentiation, however, requires extensive analysis,

(36) Grosvenor, A. P.; Kobe, B. A.; Biesinger, M. C.; McIntyre, N. S. *Surf. Interface Anal.* **2004**, *36*, 1564.
(37) Fujii, T.; de Groot, F. M. F.; Sawatzky, G. A.; Voogt, F. C.; Hibma, T.; Okada, K. *Phys. Rev. B* **1999**, *59*, 3195.

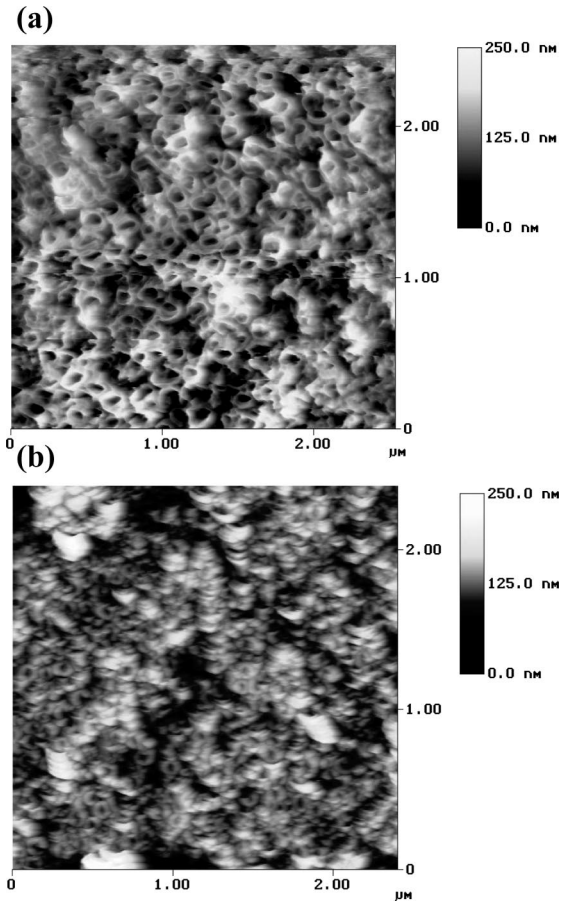

Figure 2. Top-view AFM images of (a) the unmodified TiO_2 NTs, and (b) the Fe_xO_y/TiO_2 NTs (5 mg/mL solution).

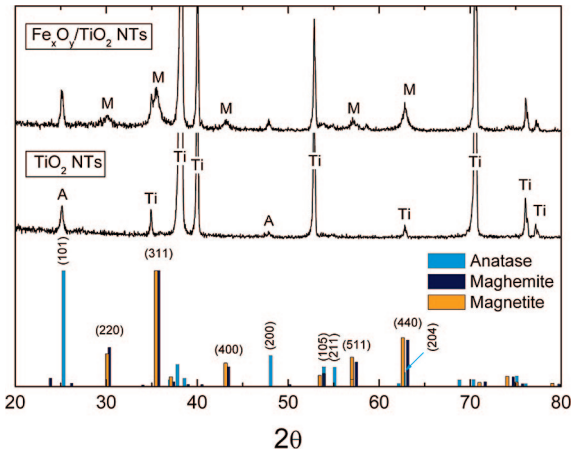

Figure 3. XRD patterns of the Fe_xO_y/TiO_2 NTs compared to the unmodified TiO_2 NTs and the standard powder patterns of anatase TiO_2, maghemite (γ-Fe_2O_3) and magnetite (Fe_3O_4).

hardly attainable within the present spectral resolution. In this case, other experimental techniques such as Mössbauer or Raman spectroscopy (vide infra) are required for identifying clearly the materials composition.[38]

The phase composition of the Fe_xO_y/TiO_2 NT nanocomposite was accordingly investigated by micro-Raman spectroscopy utilizing variable excitation wavelengths. Figure 5 shows two micro-Raman spectra of the modified TiO_2 NTs compared to

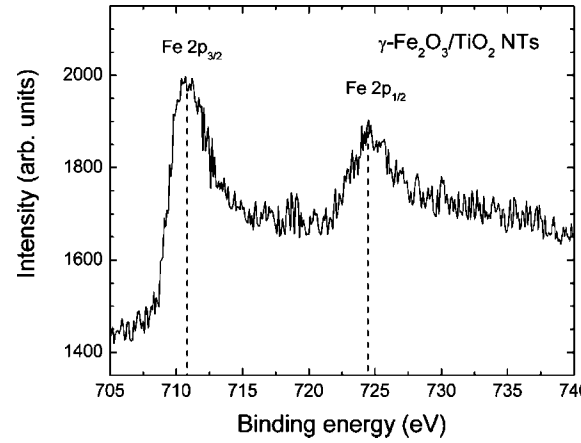

Figure 4. The XPS Fe 2p core-level spectra of the modified Fe_xO_y/TiO_2 NTs.

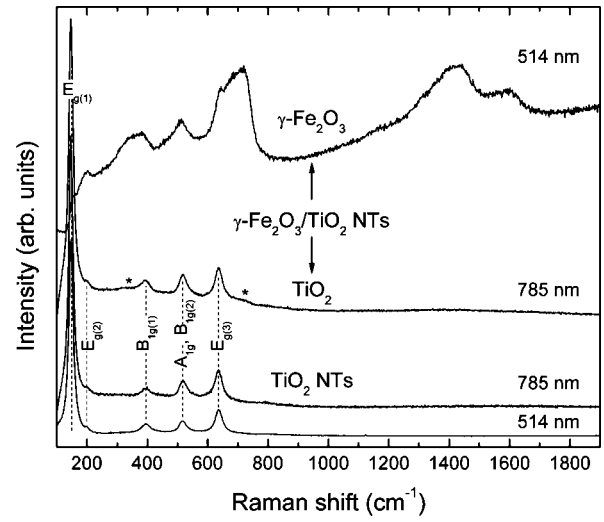

Figure 5. Resonance micro-Raman spectra of the Fe_xO_y/TiO_2 NTs compared to the unmodified TiO_2 NT arrays at excitation wavelengths of 785 nm (NIR) and 514 nm (vis). Dashed vertical lines identify the Raman modes of the anatase TiO_2 phase.

the spectrum of a bare NT layer at excitation wavelengths of 785 nm (NIR) and 514 nm (vis) and low laser power (<0.6 mW) in order to avoid local heating effects. The Raman spectrum of the unmodified NTs exhibits the vibrational modes of the anatase phase.[39,40] The tetragonal structure of anatase, space group $D_{4h}^{19}(I4_1/amd)$, leads to six Raman-active transitions: three E_g modes centered at 144, 197, and 639 cm^{-1}, two B_{1g} modes at 399 and 519 cm^{-1}, and one mode of A_{1g} symmetry at 513 cm^{-1} overlapping with the B_{1g} mode at 519 cm^{-1}.[39] Fitting the Raman spectra to a mixture of Lorentzian and Gaussian line shapes, results in the following values for the Raman frequencies and the full width at half-maximum (fwhm) given in parentheses: 145.4 (16.9), 198.9(15.3), 395.6 (30.1), 518.3(27.4), and 635.3 (30.9) cm^{-1}. These values are typical for nanocrystalline anatase with an average crystallite size below 10 nm, according to the phonon confinement model, though oxygen nonstoichiometry and/or shape effects induced by the presence of cylindrical crystallites may also be present.[40] Likewise, the NIR Raman spectra of the Fe_xO_y/TiO_2 NTs show

(38) Biddlecombe, G. B.; Gun'ko, Y. K.; Kelly, J. M.; Pillai, S. C.; Coey, J. M. D.; Venkatesan, M.; Douvalis, A. P. *J. Mater. Chem.* **2001**, *11*, 2937.

(39) Ohsaka, T.; Izumi, F.; Fujiki, Y. *J. Raman Spectrosc.* **1978**, *7*, 321.

(40) Likodimos, V.; Stergiopoulos, T.; Falaras, P.; Kunze, J.; Schmuki, P. *J. Phys. Chem. C* **2008**, *112*, 12687.

the nanocrystalline anatase vibrational modes and, additionally, the presence of two broad shoulders at about 320 and 710 cm^{-1}, depicted by asterisks (*) in Figure 5. However, a marked variation of the Raman spectrum occurs at the excitation wavelength of 514 nm, where the peaks corresponding to the anatase modes become smeared out and several broad bands extending up to high wavenumbers appear. Specifically, three broad bands around 350, 510, and 700 cm^{-1} emerge. They are a characteristic feature of the iron-deficient spinel phase of γ-Fe_2O_3,[41] along with two higher frequency broad bands at 1420 and 1600 cm^{-1}, frequently observed in maghemite as well, though possibly related to carbonaceous species.[42] The presence of γ-Fe_2O_3 nanoparticles decorating the upper NT walls of the modified TiO_2 arrays can be thus reliably inferred, so that the nanocomposite can be hereafter referred to as γ-Fe_2O_3/TiO_2 NTs. This variation is characteristic of the resonance Raman scattering as the excitation energy at 514 nm (2.4 eV) approaches the bandgap (~2 eV) of maghemite,[43] causing the enhancement of the γ-Fe_2O_3 modes, which appear only as weak shoulders on the dominant anatase modes at the off-resonance conditions of the NIR Raman spectra. Specifically, switching the excitation wavelength from 785 to 514 nm, close to the maghemite absorption edge, causes a significant decrease of the laser penetration depth because of the increase in the optical absorption coefficient, providing high sensitivity to the material's surface composition.[44] This allows discriminating the surface (γ-Fe_2O_3) from the bulk (TiO_2) Raman contributions and permits a conclusive identification of the minute concentration of maghemite nanoparticles.

3.2. Photochemical Properties. To explore the potential of the γ-Fe_2O_3/TiO_2 NT nanocomposite for photoinduced applications, we have evaluated its photocatalytic activity on the degradation of the methyl orange azo-dye. Initial experiments performed in the dark did not show any significant dye adsorption effect. Figure 6a shows the photodegradation kinetics of the MO dye under UV irradiation for a series of γ-Fe_2O_3/TiO_2 NTs functionalized in different concentrations of the iron oxide solution. For solute concentrations lower than 7.5 mg/mL, the reactions obey pseudo first-order kinetics, which can be expressed by $\ln(C/C_0) = kt$ with k being the apparent first-order reaction constant, while C_0 and C are the initial and the reaction concentrations of the MO dye (Figure 6b).[45] A systematic increase of the MO photodegradation is found upon surface modification of the NT arrays at low concentrations of the dextrin coated γ-Fe_2O_3 nanoparticles, which, however, declines rapidly at concentrations higher than 5 mg/mL, where the optimum photocatalytic performance is obtained. The inset of Figure 6b shows the corresponding variation of the apparent first-order reaction constant k as a function of the concentration of the iron-oxide solution, where a prominent maximum of k is evidenced at 5 mg/mL. Moreover, comparison with the MO decomposition rate using the unmodified TiO_2 NTs, included in the same plot, shows an increase of k by about 30% at 5 mg/mL compared to the bare NT substrate. The decrease in the photocatalytic activity at higher concentrations of the γ-Fe_2O_3 solution (>5 mg/mL) suggests that a high load of iron-oxide nanoparticles may partially block the nanochannels of the NT arrays. This is supported by SEM images on γ-Fe_2O_3/TiO_2 NTs functionalized at high concentrations of the iron oxide suspension (Figure 1d). Although the NT pores remain in most cases unblocked, coverage of the TiO_2 NT walls by a dense layer of γ-Fe_2O_3 aggregates may effectively lead to a narrowing of the tube openings. This "masking" effect reduces the photocatalyst surface area and impedes the penetration of the MO solution into the NTs. On the other hand, the dispersion of the coated γ-Fe_2O_3 nanoparticles on the NT walls at lower concentrations might result in an effective improvement of the surface area that promotes photocatalysis together with the enhanced photochemical activity that will be discussed below.

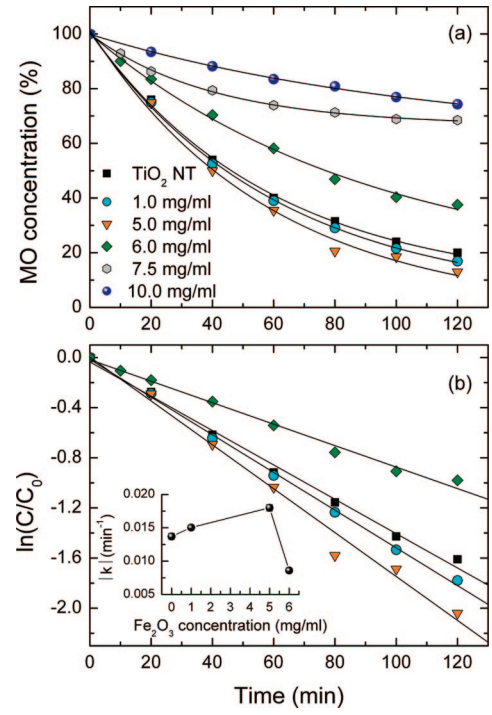

Figure 6. (a) Photodegradation kinetics of methyl orange under UV irradiation for the γ-Fe_2O_3/TiO_2 NTs functionalized in different concentrations of the iron oxide solution compared to the unmodified TiO_2 NT substrate. (b) The corresponding $\ln(C/C_0)$ vs t kinetic curves for concentrations lower than 7.5 mg/mL. The inset shows the variation of the reaction constants as a function of the concentration of the γ-Fe_2O_3 oxide solution.

To check the potential reusability and stability of the heterogeneous photocatalyst as well as possible photodissolution of the iron oxide particles in the reaction medium,[46] we have performed a series of five photocatalytic cycles using the 5 mg/mL γ-Fe_2O_3/TiO_2 NT array that exhibits the highest activity (see Figure S2 in the Supporting Information). The MO photodegradation as well as the first-order reaction constants k do not vary significantly, the results are reproducible within 5%, indicating that despite its heterogeneous

(41) de Faria, D. L. A.; Venancio Silva, S.; de Oliveira, M. T. *J. Raman Spectrosc.* **1997**, *28*, 873.
(42) Chourpa, I.; Douziech-Eyrolles, L.; Ngaboni-Okassa, L.; Fouquenet, J.-F.; Cohen-Jonathan, S.; Souce, M.; Marchais, H.; Dubois, P. *Analyst* **2005**, *10*, 1395.
(43) Cherepy, N. J.; Liston, D. B.; Lovejoy, J. A.; Deng, H.; Zhang, J. Z. *J. Phys. Chem. B* **1998**, *102*, 770.
(44) Gouadek, G.; Colomban, P. *Prog. Cryst. Growth Charact. Mater.* **2007**, *53*, 1.
(45) Kontos, A. I.; Arabatzis, I. M.; Tsoukleris, D. S.; Kontos, A. G.; Bernard, M. C.; Petrakis, D. E.; Falaras, P. *Catal. Today* **2005**, *101*, 275.

nature the photocatalyst can be safely reused. The stability of the dextrin shell under the hydroxyl radical oxidizing conditions generated during TiO_2 photocatalysis has been also evaluated by control experiments using dextrin solutions (1×10^{-4} M) without the azo-dye, under UV irradiation in the absence (self-photolysis) and the presence (photocatalysis) of the TiO_2 NT arrays. In both cases, no significant dextrin photodegradation was observed in the corresponding absorption spectra, in agreement with recent photocatalytic experiments on cyclodextrins (the cyclic counterpart of the present organic coating).[47] In this case, the chemical binding of dextrin, similar to other polyhydroxyl alcohols and carbohydrates on the TiO_2 surface via carboxyl groups, firmly established by both spectroscopic means[48,49] and theoretical work,[50] inhibits the photocatalytic decomposition of the dextrin molecules under UV irradiation. The stability of the dextrin coating was further investigated by micro-Raman measurements on γ-Fe_2O_3/TiO_2 NT arrays exposed in UV irradiation (see Figure S3 in the Supporting Information). Comparison with the micro-Raman spectra of dextrin powder at excitation wavelengths of 785 nm (NIR) and 514 nm (vis) allowed the identification of the dextrin shell in the vis-Raman spectra of γ-Fe_2O_3/TiO_2 NTs through the composite C−H bands at high wavenumbers around 2900 cm^{-1}, which are dominant at 514 nm laser excitation. No appreciable variation of the relative intensity of the dextrin-derived C−H bands could be traced in the vis-Raman spectra of γ-Fe_2O_3/TiO_2 NTs after UV irradiation, pointing to the absence of any photodegradation of the dextrin shell. In that case, no appreciable photodissolution of the iron oxide should occur, as changes in the iron oxide concentration would be directly reflected on the MO photodegradation efficiency under consecutive photocatalytic cycles. This agrees with previous results on mixed iron-oxide/TiO_2 systems where considerable photodissolution was reported only for composite samples with direct contact of the iron oxide phase with TiO_2,[46] in contrast to the noncontact conditions of the γ-Fe_2O_3 nanoparticles with the TiO_2 NT walls assured by the dextrin shell.

To explore the application potential and compare the effectiveness of the modified photocatalyst, further experiments were performed on nanoparticulate (NP) TiO_2 films, following the same functionalization route. In that case, TiO_2 NP films were prepared on Ti foils substrates (identical to that used for the TiO_2 NT anodization growth) by the doctor-blade deposition technique, using Degussa P25 TiO_2 nanopowder as precursor.[51] Figure 7 compares the MO photodegradation kinetic curves for the 5 mg/ml γ-Fe_2O_3/TiO_2 NTs with the corresponding γ-Fe_2O_3/TiO_2 NPs. A marked enhancement of the MO photodegradation is observed for the modified TiO_2 NTs over their nanoparticulate analogues,

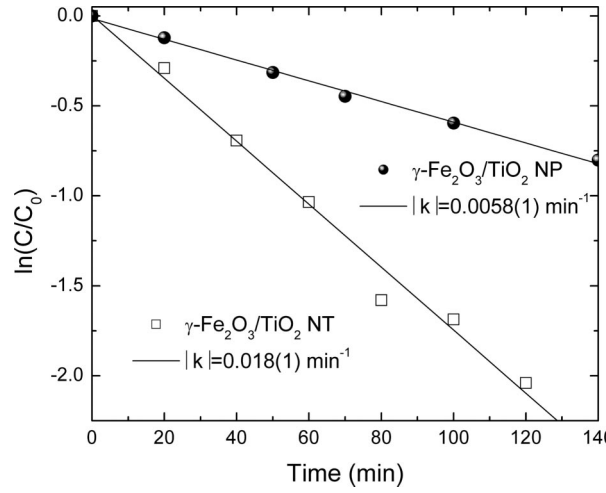

Figure 7. MO photodegradation kinetic curves of the γ-Fe_2O_3/TiO_2 NT arrays compared to the γ-Fe_2O_3/TiO_2 NP films, both modified by dipping in 5 mg/mL iron oxide solution.

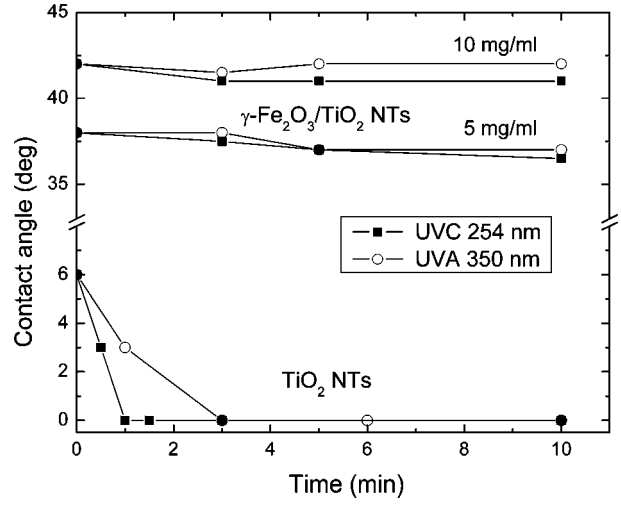

Figure 8. Variation of the water contact angle under UV illumination for the γ-Fe_2O_3/TiO_2 NTs at 5 and 10 mg/mL iron oxide concentrations, compared to the unmodified TiO_2 NT arrays.

pointing out the high photocatalytic activity of the vertically oriented nanocomposite structure.

Subsequently, the wetting properties of the nanocomposite material have been explored by advancing water contact angle (CA) measurements. Figure 8 summarizes the results of the CA as a function of time under UV illumination for the γ-Fe_2O_3/TiO_2 NTs prepared at 5 and 10 mg/mL solute concentrations in comparison with the unmodified TiO_2 NTs. Superhydrophilic behavior, that is extreme wetting with CA of ~6° is thus observed for the TiO_2 NTs, which become completely nonwater repellent after short exposure to UV radiation (CA $\approx$ 0°). This behavior complies with recent analysis of the wetting and the UV-induced superhydrophilicity of the TiO_2 NT arrays, modeled by the Cassie-Baxter mode arising from the large scale roughness of the nanotubular arrays in combination with the Wenzel mode due to the small scale roughness induced by ridges at the outer NT surface.[52,53] On the contrary, surface modification of the TiO_2

(46) Beydoun, D.; Amal, R.; Low, G. K.-C.; McEvoy, S. *J. Phys. Chem. B* **2000**, *104*, 4387.
(47) Wang, G.; Wu, F.; Zhang, X.; Luo, M.; Deng, N. *J. Hazard. Mater.* **2006**, *B133*, 85.
(48) Dimitrijevic, N. M.; Rajh, T.; Saponjic, Z. V.; de la Garza, L.; Tiede, D. M. *J. Phys. Chem. B* **2004**, *108*, 9105.
(49) Shkrob, I. A.; Sauer, M. C.; Gosztola, D. *J. Phys. Chem. B* **2004**, *108*, 12512.
(50) Du, M.-H.; Feng, J.; Zhang, S. B. *Phys. Rev. Lett.* **2007**, *98*, 066102.
(51) Arabatzis, I. M.; Stergiopoulos, T.; Bernard, M. C.; Labou, D.; Neofytides, S. G.; Falaras, P. *Appl. Catal., B* **2003**, *42*, 187.
(52) Shirtcliffe, N. J.; McHale, G.; Newton, M. I.; Perry, C. C. *Langmuir* **2005**, *21*, 937.

NTs by the dextrin coated γ-Fe_2O_3 nanoparticles resulted in a substantial reduction of the surface wettability. Even though the NT surface remained hydrophilic, the CA increased considerably to ~38 and ~41° for the 5 and 10 mg/mL γ-Fe_2O_3 solutions, exceeding the value of ~30° measured for a flat TiO_2 surface.[1,53] Such a behavior cannot be solely accounted for by the reduction of the surface area, as the γ-Fe_2O_3 nanoparticles decorate mostly the NT walls (Figure 1), suggesting that changes of the surface chemistry can be implicated, as well. Specifically, the CA increase indicates a decrease of the light induced surface hydroxylation, turning the initially superhydrophilic TiO_2 NTs surface to a less hydrophilic state. This may be further controlled by varying the iron oxide loading on the NT surface and the possibility to selectively modify the nanoparticle charge in the iron oxide colloidal precursor solution. Most importantly, the high photocatalytic activity of the nanocomposite is accompanied by a significant hydrophobic transformation of the NT surface, fact that is considered of high importance in self-cleaning applications.[1] In particular, the γ-Fe_2O_3/TiO_2 nanocomposite surface simultaneously disposes enhanced photocatalytic and moderate hydrophilic character, both determining its self-cleaning ability. The first functionality stems from the semiconducting TiO_2 nanotubular arrays and depends on the interaction with light, whereas the second one is characteristic of the iron oxide nanoparticulate component and remains practically unaffected by light, leading to the effective separation of the photocatalytic from the wetting behavior in the γ-Fe_2O_3/TiO_2 NT nanocomposite.

To investigate further the photochemical activity of the TiO_2 NT arrays upon deposition of the γ-Fe_2O_3 nanoparticles, we have measured the diffuse-reflectance (DR) UV−vis spectra of the modified γ-Fe_2O_3/TiO_2 NT arrays (see Figure S4 in the Supporting Information). Comparison with the DR UV−vis spectra of the unmodified TiO_2 NTs shows no substantial variation of the optical absorbance in the UV range for the γ-Fe_2O_3/TiO_2 NTs (the absorption edge remains intact even after deposition of the 10 mg/mL γ-Fe_2O_3 solution), indicating that there is no mass/volume doping, whereas the concentration of the maghemite nanoparticles is low enough to significantly affect the optical response of the composite system.

3.3. Electrochemical Properties. Electrochemical impedance spectroscopy (EIS) is an effective tool for probing the features of surface-modified electrodes and was further employed to analyze the semiconducting properties (transport included) of the γ-Fe_2O_3/TiO_2 NTs electrodes. Figure 9 shows the EIS spectra (Nyquist plots, corresponding to the imaginary part Z'' vs the real part Z' of the complex impedance Z) measured in aqueous 0.1 M Na_2SO_4 solution for the 5 mg/mL γ-Fe_2O_3/TiO_2 NT array, exhibiting the highest photocatalytic activity, in comparison with the unmodified TiO_2 NT substrate. Both samples show a pronounced arc (semicircle portion) at higher frequencies in the EIS plane, whose diameter corresponds to the electron-transfer resistance controlling the kinetics at the electrode

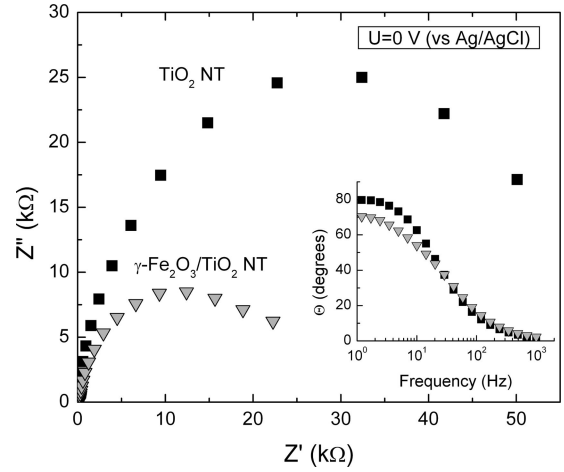

Figure 9. EIS Nyquist plots for the γ-Fe_2O_3/TiO_2 NT array (5 mg/mL γ-Fe_2O_3) in comparison with the unmodified TiO_2 NT substrate. The inset shows the corresponding variation of the phase angle as a function of frequency (Bode plot) for the two samples.

interface.[54,55] Significant changes in the EIS spectra are observed for the TiO_2 NT electrodes, following iron oxide modification. In fact, deposition of the γ-Fe_2O_3 nanoparticles on the TiO_2 NTs results in a marked decrease of the semicircle diameter, that justifies an analogous decrease of the electron-transfer resistance and relates directly to the accessibility of the underlying electrode or the film permeability. This behavior is also supported by the frequency dependence of the phase angle (Bode plot) shown in the inset of Figure 9. In this case, an appreciably larger deviation of the phase angle (Θ) from the purely capacitive behavior ($\Theta = -90°$) is observed at low frequencies for the γ-Fe_2O_3/TiO_2 NT arrays ($\Theta \approx -70°$) indicative of the introduction of a more conductive medium on the TiO_2 NT electrode. It should be noted that such behavior may be related to the advantageous trapping of excited electrons from metal particles residing on the TiO_2 surface.[51] However, this is not supported by the XPS and Raman results, where no metallic iron particles could be identified on the modified NT surface, excluding the possibility of metal promoted photocatalytic activity. In this case, the enhanced performance of the γ-Fe_2O_3/TiO_2 NTs could originate from the improvement of charge carrier separation, as recently reported for S-doped titanate nanotubes loaded with iron oxide nanoparticles[31] and surface conjugated polyhydroxyl molecules on TiO_2 nanoparticles.[48,49]

To explore further the above hypothesis, Mott−Schottky (MS) measurements were performed by using the impedance technique at 30 Hz, which falls within the capacitive regime of the Bode plot (see inset of Figure 9). The system's capacitance C is then calculated from the imaginary part of the impedance: $C = -1/\omega Z''$. Figure 10 shows the corresponding MS plots for the 5 mg/mL γ-Fe_2O_3/TiO_2 NT array, compared to the unmodified TiO_2 NT substrate. Both samples exhibit reversed sigmoidal plots with an overall shape consistent with *n*-type semiconductors with no ap-

(53) Kontos, A. G.; Kontos, A. I.; Tsoukleris, D. S.; Likodimos, V.; Kunze, J.; Schmuki, P.; Falaras, P. *Nanotechnology* **2009**, *20*, 045603.

(54) Tse, K.-Y.; Nichols, B. M.; Yang, W.; Butler, J. E.; Russell, J. N., Jr.; Hamers, R. J. *J. Phys. Chem. B* **2005**, *109*, 8523.

(55) Leng, W. H.; Zhang, Z.; Zhang, J. Q.; Cao, C. N. *J. Phys. Chem. B* **2005**, *109*, 15008.

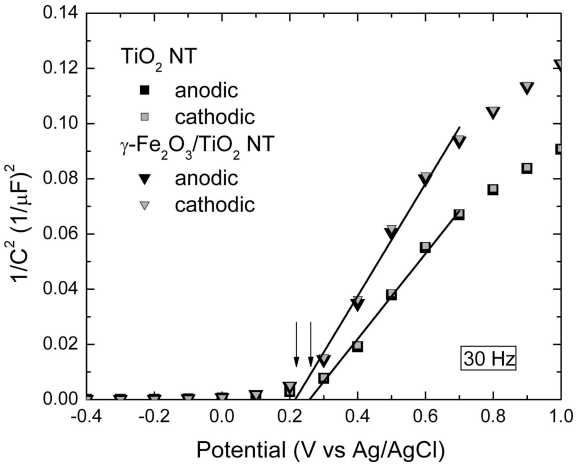

Figure 10. Mott−Schottky plots for the γ-Fe_2O_3/TiO_2 NT array (5 mg/mL γ-Fe_2O_3) and the unmodified TiO_2 NT substrate, measured at 30 Hz in 0.1 M Na_2SO_4 solution. Arrows and lines depict the zero-intercept (flat-band potential) and the linear fits to the MS curves for the two samples.

preciable hysteresis in anodic and cathodic (forward and backward) scans. The MS plots are linear in the potential range from +0.25 to +0.7 V vs Ag/AgCl. According to the Mott−Schottky analysis, the space charge capacitance C_{sc} of the doped semiconductor in the depletion zone, valid under biasing conditions, is expressed as

$$\frac{1}{C_{sc}^2} = \frac{2}{e\varepsilon\varepsilon_0 N_D}\left(U - U_{fb} - \frac{k_B T}{e}\right)$$

where e is the electronic charge, N_D is the dopant (donor) density, ε_0 is the permittivity of free space, ε the dielectric constant of the anodic film, U_{fb} is the flat band potential, and k_B is the Boltzmann constant. In the case of a linear MS plot, the flat band potential can be readily determined from the x-intercept when $1/C_{sc}^2 = 0$.[56] A negative intercept shift is observed for the γ-Fe_2O_3/TiO_2 NT arrays, indicating a decrease of the flat band potential. This indicates a shift of the conduction band of the composite semiconductor to more positive potentials, which matches better the redox potential of $O_2/O_2^{\bullet-}$ promoting the formation of $O_2^{\bullet-}$ radicals able to decompose organic pollutants. The observed E_{fb} variation could be also due to a change in the surface chemistry of TiO_2 NT walls and the concomitant modification of the surface states mediating charge transfer. In fact, the flat band potential of TiO_2 is known to depend strongly on the surface chemical nature, in particular on the pH-dependent hydroxyl concentration.[57] In agreement with the above results, the increase of the water contact angle observed for the γ-Fe_2O_3/TiO_2 NT arrays is a signal of poorer surface hydroxylation.

Composite semiconductor systems of Fe_2O_3/TiO_2 under simultaneous light activation, have been predicted to promote vectorial interparticle charge transfer from TiO_2 to Fe_2O_3 as both the valence and conduction bands of the iron-oxide fall within the band gap of TiO_2.[58] In that case, deterioration of the performance of the coupled photocatalyst has been reported due to the inferior photocatalytic efficiency of Fe_2O_3, which is severely hindered by the low optical absorption coefficients and the short hole diffusion length (2−4 nm), leading to the fast relaxation of photoexcited electrons and rapid electron−hole recombination for both α and γ-Fe_2O_3 polymorphs.[43,59] This detrimental effect in the photocatalytic activity of coupled Fe_2O_3/TiO_2 systems, has been partially circumvented by the addition of a thin SiO_2 membrane between a γ-Fe_2O_3 core and a TiO_2 shell, proposed for the synthesis of magnetically separable photocatalysts, where the silica membrane inhibited to some extent the injection of electrons from TiO_2 to γ-Fe_2O_3 particles.[60] On the other hand, polyhydroxyl dextrin molecules chemically grafted on TiO_2 have been recently shown to scavenge photogenerated holes very efficiently,[48,49] most likely through the formation of localized states above the semiconductor valence band edge that act as hole traps,[50] and permit charge transfer and strong electronic coupling between the constituent nanocrystalline oxides of the γ-Fe_2O_3/TiO_2 NT composite. In this case, holes excited by UV illumination from the TiO_2 NTs during the photocatalytic reaction can be rapidly transferred to the γ-Fe_2O_3 nanoparticles, where dextrin molecules can be also efficiently anchored,[61] promoting interfacial charge separation. Based on the results of the impedance/capacitance measurements, confirming a characteristic decrease of the electron transfer resistance and appreciable variations of the surface state properties for the γ-Fe_2O_3/TiO_2 NT arrays, the enhanced photocatalytic activity can be related to more efficient charge separation at low loading of the γ-Fe_2O_3 nanoparticles triggered by the dextrin shell mediating charge transfer from TiO_2 to Fe_2O_3 regions.

The role of the dextrin coating is also supported by the reduction of the MO photodegradation rate for the γ-Fe_2O_3/TiO_2 NTs after postannealing at 500 °C, where dextrin decomposes. Figure 11a, compares the NIR and vis-Raman spectra of the γ-Fe_2O_3/TiO_2 NT arrays after annealing at 500 °C and low laser power (∼0.1 mW) to avoid local heating effects. In that case, the broad Raman modes of γ-Fe_2O_3 are replaced by a series of well-defined Raman peaks, particularly prominent in the vis-Raman spectra, where the anatase TiO_2 modes are hardly discerned. These bands can be identified with the Raman-active modes of hematite [space group D_{3d}^6 ($R\bar{3}c$)] at 226.3 (A_{1g}), 247 (E_g), 294 (E_g), 299(E_g) 412 (E_g), 499 (A_{1g}), 613 (E_g) cm^{-1}, the disorder-induced mode at 665 cm^{-1} and its second order overtone at 1320 cm^{-1},[41,42] revealing the phase transformation of the nanocomposite system to α-Fe_2O_3/TiO_2 NTs. Moreover, their intensity at 514 nm exceeds largely that of the anatase Raman modes because of the resonance of the laser excitation energy (2.14 eV) with the hematite (α-Fe_2O_3) band gap (∼2.2 eV). Figure 11b compares the photocatalytic activity of the nanocomposites before and after post thermal treatment at 500 °C for the MO degradation. A marked drop of the MO photodegradation rate is observed for the α-Fe_2O_3/TiO_2 NTs (k decreases by about 43%), further suggesting that the

(56) Nozik, A. G.; Memming, R. *J. Phys. Chem.* **1996**, *100*, 13061.
(57) Munoz, A. G. *Electrochim. Acta* **2007**, *52*, 4167.
(58) Serpone, N.; Maruthamuthu, P.; Pichat, P.; Pelizzetti, E.; Hidaka, H. *J. Photochem. Photobiol. A: Chem.* **1995**, *85*, 247.
(59) Kay, A.; Cesar, I.; Grätzel, M. *J. Am. Chem. Soc.* **2006**, *128*, 15714.
(60) Chen, F.; Xie, Y.; Zhao, J.; Lu, G. *Chemosphere* **2001**, *44*, 1159.
(61) Rajh, T.; Chen, L. X.; Lukas, K.; Liu, T.; Thurnauer, M. C.; Tiede, D. M. *J. Phys. Chem. B* **2002**, *106*, 10543.

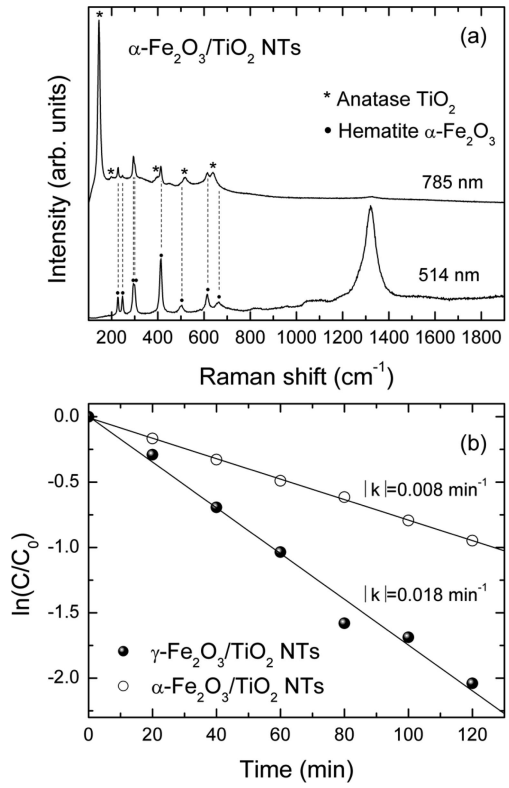

Figure 11. (a) Resonance micro-Raman spectra of the Fe_xO_y/TiO_2 NTs after post-thermal annealing at 500 °C at 785 nm (NIR) and 514 nm (vis), showing the phase transformation to α-Fe_2O_3/TiO_2 NTs. The anatase (TiO_2) and hematite (α-Fe_2O_3) Raman modes are indicated by asterisks and dots, respectively. (b) MO photodegradation kinetic curves of the α-Fe_2O_3/TiO_2 NTs compared to γ-Fe_2O_3/TiO_2 NT arrays.

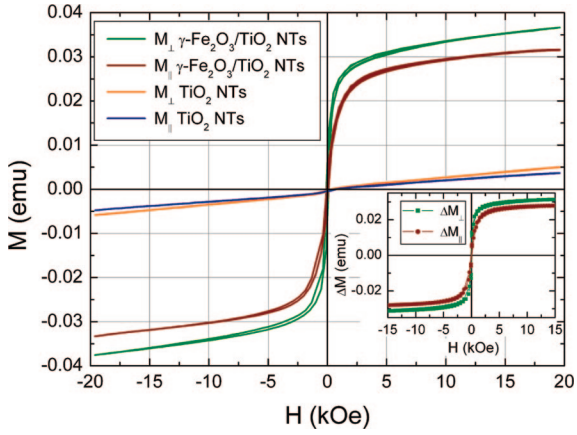

Figure 12. Magnetization loops for the γ-Fe_2O_3/TiO_2 NTs compared to a bare TiO_2 NT sample, with the magnetic field applied parallel and perpendicular to the tube axis. The inset shows the corresponding curves after subtraction of the contribution of the TiO_2 NT substrate.

dextrin coating of the iron-oxide nanoparticles plays a crucial role in attaining a high photocatalytic activity.

3.4. Magnetic Properties. Figure 12 shows the magnetization loops for the modified γ-Fe_2O_3/TiO_2 NTs in comparison with an unmodified titania NT sample, with the magnetic field applied parallel and perpendicular to the tube axis. Ferromagnetic response is observed for the γ-Fe_2O_3 decorated NTs, superimposed on a weak magnetic background of the NT substrate, most likely caused by paramagnetic defects and ferromagnetic impurities. Subtraction of the latter contribution M_{TiO_2} from the total magnetization M_{tot} of the nanocomposite, reveals clear ferromagnetic, hysteretic behavior of $\Delta M = M_{tot} - M_{TiO_2}$ as a function of the magnetic field with appreciable anisotropy (the saturation magnetization increases by about 13% in the perpendicular configuration) and small coercivity, the coercive field being about 70 and 90 Oe when the external field is applied parallel and perpendicular to the NT axis, respectively, excluding plain superparamagnetism. Although the observation of nonzero coercivity can be related to the formation of maghemite aggregates, whose magnetic moment remains blocked at room temperature, the presence of magnetic anisotropy, resembling to some extent that of aligned carbon nanotube arrays filled with short Fe nanowires,[62] implies an additional magnetic functionality that might be brought up by the dipolar coupling of the individual nanoparticles arranged at the top walls of the packed NTs.

4. Conclusions

We have demonstrated the surface functionalization of self-organized TiO_2 NT arrays by dextrin coated iron oxide nanoparticles, providing a composite vertically oriented nanostructure. Detailed study of the surface morphology, phase composition, and structural properties of this oxide nanocomposite reveals successful decoration of the upper nanotube walls by γ-Fe_2O_3 nanoparticles. Investigation of the material's photochemical properties, shows that the γ-Fe_2O_3/TiO_2 NT nanocomposite not only sustains the photoinduced activity of the TiO_2 NT substrate but exhibits high photocatalytic performance at relatively low deposition levels of γ-Fe_2O_3 nanoparticles. In addition, effective separation of the photocatalytic action from the surface wettability is achieved, while attaining an additional functionality through the magnetic field response of the iron-oxide component that shows appreciable magnetization anisotropy parallel and perpendicular to the tube axis. Electrochemical impedance and Mott−Schottky analysis confirmed a characteristic improvement of the interfacial electron-transfer kinetics for the γ-Fe_2O_3/TiO_2 NT arrays at low loads of the iron-oxide nanoparticles and enhanced charge carrier separation, attributed to the unique hole scavenging ability of the polyhydroxyl dextrin shell that allows charge transfer between the constituent semiconductor oxides. This leads to the enhanced photocatalytic activity over azo-dyes and the conversion of the initially superhydrophilic NT surface to a less hydrophilic one. Exciting prospects for technological applications, combining the different independent functionalities (photocatalytic, wetting, magnetic) of the oxide nanomaterials supported in the vertically oriented NT structure, could be envisaged.

Acknowledgment. This work is undertaken in the Ti-Nanotubes project, "Preparation, Characterization and Application of Self-Organized Titanium Oxide - Nanotubes", supported under Contract NMP4-CT-2006-033313 by the Nanotechnologies Materials and Production technologies (NMP) programme of the Sixth Framework Programme for Research and Technological Development. The authors gratefully acknowledge the

(62) López-Urías, F.; Muñoz-Sandoval, E.; Reyes-Reyes, M.; Romero, A. H.; Terrones, M.; Morán-López, J. L. *Phys. Rev. Lett.* **2005**, *94*, 216102.

GSRT/Ministry of Development-Greece (03EΔ118/2005PENED and 4.5/4.4.1 Competitiveness/Infrastructure-EPAN YPODOMON projects) for financial support. Helpful assistance from M. C. Bernard (diffuse reflectance UV−vis spectra) and Prof. T. Karakostas (TEM measurements) is highly acknowledged.

Supporting Information Available: High-magnification SEM images of 5 mg/mL γ-Fe_2O_3/TiO_2 NTs. Methyl orange photodegradation yield and kinetic reaction constants after five successive photocatalytic cycles using the 5 mg/mL γ-Fe_2O_3/TiO_2 NTs under identical reaction conditions. Micro-Raman spectra of the γ-Fe_2O_3/TiO_2 NTs before and after UV irradiation at 254 nm for 90 min and dextrin powder at 514 and 785 nm. UV−vis absorbance spectra of the γ-Fe_2O_3/TiO_2 NTs compared to the unmodified TiO_2 nanotube substrate (PDF). This material is available free of charge via the Internet at http://pubs.acs.org.

CM802495P